Interfacial shear stress optimization in sandwich beams with polymeric core using non-uniform distribution of reinforcing ingredients

Hamid Ghasemi**[1], Pierre Kerfriden[2], Stéphane P. A. Bordas[2], J. Muthu[3], Goangseup Zi[4], Timon Rabczuk*[1, 4]

[1] Institute of Structural Mechanics, Bauhaus University Weimar, Marienstraße 15, 99423 Weimar, Germany
[2] Institute of Mechanics and Advanced Materials, Cardiff University, Cardiff CF 24 3AA, UK
[3] School of Mechanical, Industrial and Aeronautical Eng., Uni. of the Witwatersrand, WITS 2050, S. Africa
[4] School of Civil, Environmental and Architectural Eng., Korea University, Seoul, S. Korea

Abstract

Core shearing and core/face debonding are two common failure states of sandwich beams which are mainly the result of excessive shear stresses in the core. Generally, the core made of homogeneous Fiber Reinforced Polymer (FRP) shows better shear resistance in comparison with that made of pure polymer. Usually, this enhancement is however somewhat limited. This paper proposes a methodology to decrease interfacial stresses by presenting the optimal distribution of reinforcing ingredients in the polymeric matrix. For this purpose, a Non-Uniform Rational B-spline (NURBS) based reinforcement distribution optimizer is developed. This technique aims at the local stress minimization within any arbitrary zone of the design domain. In our methodology, optimization and model analysis (calculation of the objective function and the design constraints) have common data sets. The quadratic NURBS basis functions smoothly define the reinforcement distribution function as a NURBS surface. The core and face sheets are modeled as multi-patches and compatibility in the displacement field is enforced by the penalty method. An adjoint sensitivity method is devised to minimize the objective function within areas of interest defined over arbitrary regions in the design domain. It is also used for efficient updating of design variables through optimization iterations. The method is verified by several examples.

Keywords: Optimization, Sandwich beam, NURBS, Material interface, Isogeometric Analysis (IGA)

1. Introduction

Sandwich beams are a special class of composite materials fabricated by attaching two thin but stiff face sheets to a lightweight thick core which experiences mostly shear stresses. As a result of

---

*Corresponding Author: Tel: (+49)3643-584511, E-Mail: timon.rabczuk@uni-weimar.de
**Corresponding Author: E-Mail: hamid.ghasemi@uni-weimar.de

their high bending stiffness and high strength to weight ratios, sandwich beams have numerous applications in the automotive, aerospace, marine and construction industries [1]. A comprehensive review and assessment of various theories for modeling sandwich composites are presented in [2]. Core shearing and debonding between core and face sheets are two common failure modes of these structures. Core shearing occurs when a sandwich beam is subjected to an excessive transverse shear force. Moreover, experimental evidence shows that debonding failure is influenced by the existence of a crack at the imperfect interface [3]. The excessive interfacial stresses between the core and the face sheet can be considered as a main cause for this failure.

To decrease the stress concentration at the interface, Functionally Graded Materials (FGMs) with continuously varying composition have been developed [4]. However, FRP materials are also widely used in the core of sandwich beams. Improving the interfacial stresses within FRP cores were only superficially studied. Available research on interfacial stresses optimization mainly concerns beams strengthened with FRP bonded plate. For instance, Krour et al. [5] and Lousdad et al. [6] tried to minimize interfacial stresses of a concrete beam strengthened with FRP plate, by finding optimal fiber orientation in the FRP plate and its end shape, respectively.

Motivated by our previous research on fiber distribution optimization in Fiber Reinforced Composite (FRC) structures [7], we extend the methodology to present an optimization package for sandwich beams minimizing any stress state within any arbitrary area of interest defined over the design domain. The advantages of our methodology include: The same data set is used for optimization and analysis, high convergence rate due to the smoothness of the NURBS, mesh independency of the optimal layout, no need for any post processing technique and its non-heuristic nature (see [7]). In our present work we also devise an adjoint sensitivity technique for flexible choice of regions where the stress reduction is demanded. The technique is used for efficient updating of the design variables during optimization iterations.

The remainder of this paper is organized as follows: In Section 2 and Section 3, FGMs and IGA fundamentals are briefly discussed. Material discontinuity and optimization methodology are explained in Section 4 and 5, respectively. Afterwards, case studies in Section 6 and concluding remarks in Section 7 are presented.

2. Short introduction to FGM and homogenization technique

Mechanical characteristics at any point in FGMs depend on the volume fraction of its ingredients. The sum of the volume fraction of reinforcement (V_c) and the matrix (V_m) is equal to unity ($V_m + V_c = 1$). In a beam with a FG core, the volume fraction of reinforcement is assumed to follow the power law distribution:

$$V_c = \left(\frac{1}{2} + \frac{y}{t_c}\right)^n \qquad \text{with} \qquad n \geq 0 \qquad (1)$$

where n is a non-negative exponent, y is the distance from the midline of the core in the thickness direction and t_c is the FG core thickness. Fig.1 depicts V_c versus the non dimensional thickness $\frac{y}{t_c}$, for different values of n. It is clear the mechanical properties of the FG core significantly depend on n.

For the sake of simplicity, the rule of mixtures as a classical homogenization approach is used in this work. The Mori-Tanaka homogenization technique [8] is also used for model verification purposes. A summary of the governing equations can be stated as follows:
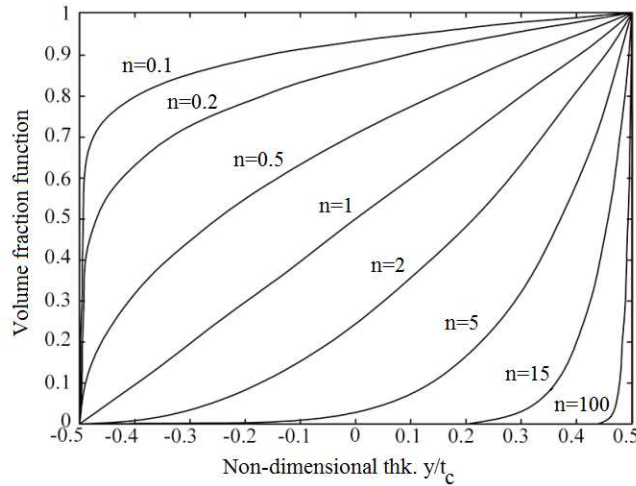
Fig.1 Volume fraction versus the non-dimensional thickness for various n of the FG core, figure from [9]

Rule Of Mixtures (ROM) method:

$$P_{eff} = P_m V_m + P_c V_c \qquad (2)$$

By substituting Eq.(1) in to Eq.(2) the effective Young's modulus E_{eff}, Poisson's ratio ν_{eff} and mass density ρ_{eff} of the FG core are determined by :

$$E_{eff} = E_m V_m + E_c V_c = (E_C - E_m)\left(\frac{1}{2} + \frac{y}{t_c}\right)^n + E_m \qquad (3a)$$

$$\nu_{eff} = \nu_m V_m + \nu_c V_c = (\nu_C - \nu_m)\left(\frac{1}{2} + \frac{y}{t_c}\right)^n + \nu_m \qquad (3b)$$

$$\rho_{eff} = \rho_m V_m + \rho_c V_c = (\rho_C - \rho_m)\left(\frac{1}{2} + \frac{y}{t_c}\right)^n + \rho_m \qquad (3c)$$

Mori-Tanaka method:

In contrast to the ROM, the Mori-Tanaka scheme considers the forces between the matrix and particulate phases and accounts for the interaction of the elastic fields among neighboring inclusions [8]. The effective bulk modulus K_{eff} and the effective shear modulus G_{eff} of a mixture of two constituents are determined by [9]:

$$\frac{K_{eff} - K_c}{K_m - K_c} = \frac{V_m}{1 + (1 - V_m)\widetilde{K}} \qquad \text{with} \qquad \widetilde{K} = \left(\frac{K_m - K_c}{K_c + \frac{4}{3}G_c}\right) \qquad (4a)$$

$$\frac{G_{eff} - G_c}{G_m - G_c} = \frac{V_m}{1 + (1 - V_m)\widetilde{G}} \qquad \text{with} \qquad \widetilde{G} = \left(\frac{G_m - G_c}{G_c + \frac{G_c(9K_c + 8G_c)}{6(K_c + 2G_c)}}\right) \qquad (4b)$$

where (K_c, G_c) and (K_m, G_m) are the bulk and the shear modulus of the reinforcement and matrix constituents respectively, obtained by:

$$K_l = \frac{E_l}{3(1 - 2\nu_l)} \; ; G_l = \frac{E_l}{2(1 + \nu_l)} \qquad \text{with} \qquad l = m, c \qquad (5)$$

Finally, the effective Young's (E_{eff}) modulus and Poisson's ratio (ν_{eff}) are given by:

$$E_{eff} = \frac{9K_{eff}G_{eff}}{3K_{eff} + G_{eff}} \qquad \text{and} \qquad \nu_{eff} = \frac{3K_{eff} - 2G_{eff}}{2(3K_{eff} + G_{eff})} \qquad (6)$$

3. Fundamentals of IGA

IGA was introduced by T.J.R. Hughes and co-workers to unify Computer Aided Design (CAD) and Computer Aided Engineering (CAE) [10]. Instead of Lagrange polynomial, CAD-shape functions are used in IGA for Finite Elements (FE) analysis. Using IGA concepts, shape optimization can be performed by the designer directly from the CAD model, without generating or regenerating any mesh to discretize the domain [11, 12].

The predominant technology which is widely used by CAD in order to represent complex geometries is NURBS. Its basis is given by

$$R_i^p(\xi) = \frac{N_{i,p}(\xi)w_i}{W(\xi)} = \frac{N_{i,p}(\xi)w_i}{\sum_{i'=1}^n N_{i',p}(\xi)w_{i'}} \tag{7a}$$

where $N_{i,p}(\xi)$ are B-spline basis functions recursively defined by using Cox-de Boor formula and starting with piecewise constants $(p = 0)$ [13]

$$N_{i,0}(\xi) = \begin{cases} 1 & if \ \xi_i \le \xi < \xi_{i+1} \\ 0 & otherwise \end{cases} \tag{7b}$$

and for $p = 1,2,3, ...$

$$N_{i,p}(\xi) = \frac{\xi - \xi_i}{\xi_{i+p} - \xi_i} N_{i,p-1}(\xi) + \frac{\xi_{i+p+1} - \xi}{\xi_{i+p+1} - \xi_{i+1}} N_{i+1,p-1}(\xi) \tag{7c}$$

w_i is also referred to as the ith weight while $W(\xi)$ is weighting function defined as follows:

$$W(\xi) = \sum_{i=1}^n N_{i,p}(\xi)w_i \tag{7d}$$

Applying the quotient rule to Eq.(7a) yields:

$$\frac{d}{d\xi} R_i^p(\xi) = w_i \frac{W(\xi)N_{i,p}^{'}(\xi) - W'(\xi)N_{i,p}(\xi)}{(W(\xi))^2} \tag{8a}$$

with

$$N_{i,p}^{'}(\xi) = \frac{p}{\xi_{i+p} - \xi_i} N_{i,p-1}(\xi) - \frac{p}{\xi_{i+p+1} - \xi_{i+1}} N_{i+1,p-1}(\xi) \tag{8b}$$

and

$$W'(\xi) = \sum_{i=1}^n N'_{i,p}(\xi)w_i \tag{8c}$$

If the weights are all equal, then $R_i^p(\xi) = N_{i,p}(\xi)$; hence, B-splines are special cases of NURBS. Finally, a NURBS curve is defined as:

$$C(\xi) = \sum_{i=1}^n R_i^p(\xi)B_i \tag{9a}$$

where $B_i \in \mathbb{R}^d$ are control points and $i = 1,2, ..., number\ of\ control\ points$. Similarly, for definition of a NURBS surface, two knot vectors $E = \{\xi_1, \xi_2, ..., \xi_{n+p+1}\}$ and $H = \{\eta_1, \eta_2, ..., \eta_{m+q+1}\}$ (one for each direction) as well as a control net $B_{i,j}$ are required. A NURBS surface is defined as:

$$S(\xi, \eta) = \sum_{i=1}^n \sum_{j=1}^m R_{i,j}^{p,q}(\xi, \eta)\,B_{i,j} \tag{9b}$$

where $R_{i,j}^{p,q}(\xi,\eta)$ is constructed according to

$$R_{i,j}^{p,q}(\xi,\eta) = \frac{N_{i,p}(\xi)M_{j,q}(\eta)w_{i,j}}{\sum_{i'=1}^{n}\sum_{j'=1}^{m}N_{i',p}(\xi)M_{j',q}(\eta)w_{i',j'}} \qquad (10)$$

where $N_{i,p}(\xi)$ and $M_{j,q}(\eta)$ are univariate B-spline basis functions of order p and q corresponding to knot vector E and H, respectively.
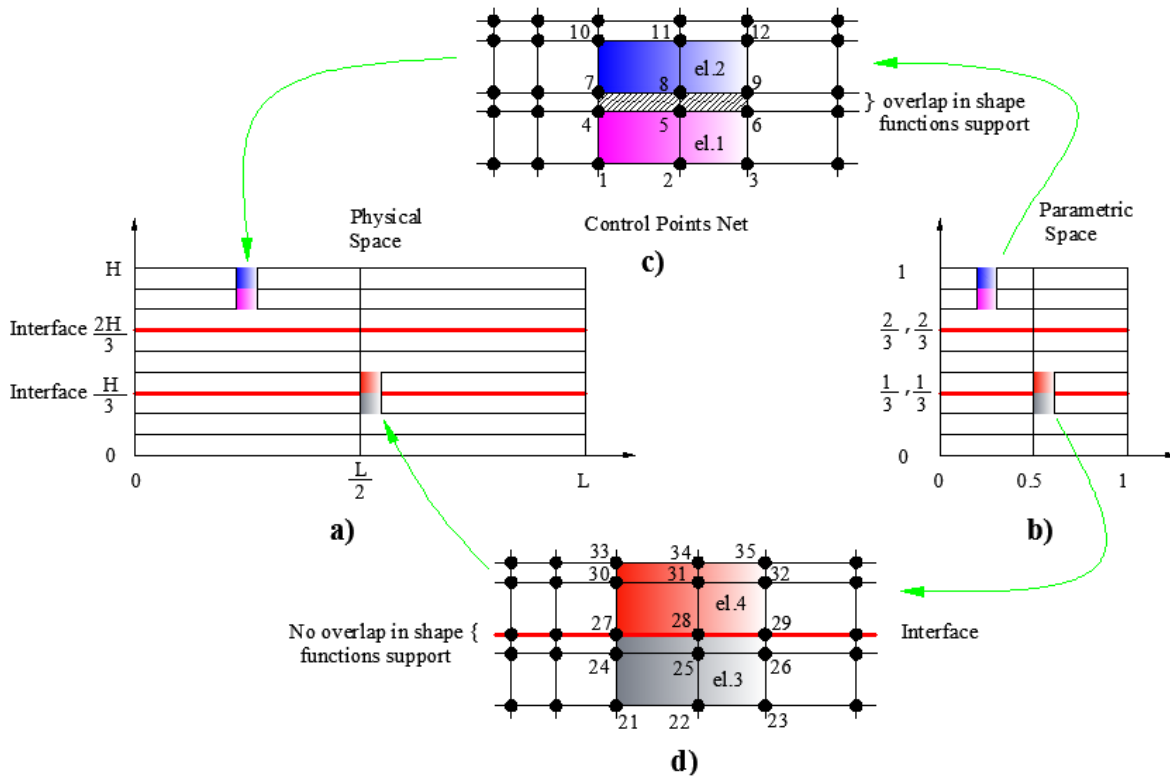
4. Material discontinuity

In a sandwich beam, material properties for the core and the face sheets are different, so the displacement solution at the interface of the core and the face sheets is only C^0 continuous and the strain field (displacement gradient) is discontinuous across the material interface. It means there is discontinuity in gradient field. In classical C^0 FEM, weak discontinuities can be automatically captured, if the material interface is located on an element boundary (conforming mesh). However, for problems with curved interfaces, using conforming meshes may be cumbersome, especially when such interfaces evolve. Several advanced methods like the Extended Finite Element Method (XFEM) [14, 15] and XIGA [16, 17] have been developed for capturing material discontinuity using non conforming mesh. Recently Nguyen proposed very simple approaches to handle such discontinuities in IGA for composite delamination using knot insertion for cohesive interfaces [18].

In IGA, continuity across an interior element boundary directly depends on the polynomial order and the multiplicity of the corresponding knot. Thus, knot insertion can be used to tailor the continuity of the fields along element interface (see Fig.2). Taking the knot vector in 1-D as $N = \{\xi_1, \xi_2, \dots, \xi_{n+p+1}\}$, where ξ_i is the ith knot, n is the number of basis functions and p is the polynomial order, the basis functions across knot ξ_i are $p - m_i$ times continuously differentiable or C^{p-m_i} continuous; where m_i is the multiplicity of knot ξ_i.

Fig.2(a) and 2(b) present the physical and parametric spaces; Fig.2(c) and 2(d) compare supports of the shape functions for interior (entirely inside the core or the face sheets) and interfacial elements. According to Fig.2(c), control points corresponding to interior element no.1 are {1, 2, 3, 4, 5, 6, 7, 8, 9} and for interior element no.2 are {4, 5, 6, 7, 8, 9, 10, 11, 12}. Two rows of control points (i.e. row {4, 5, 6} and row {7, 8, 9}) are in common between these two elements. These shared control points produce overlapping shape functions as illustrated in

Fig.2(c). In other words, the shape functions extend beyond the elements (C^1 continuity). In contrary to the interior elements, interfacial elements have at least one edge on the material interface. Two of these elements (elements no. 3 and no.4) are shown in Fig.2(d). These two elements have only one row of control points (i.e. row {27, 28, 29}) in common due to repeated knot at the interface. This knot insertion imposes C^0 continuity in the displacement field at the position of the material interface. As shown in Fig.2(d), the shape functions of elements no.3 and no.4 do not overlap with each others.


Fig.2 Schematic illustration of C^1 and C^0 continuity of quadratic NURBS elements, **a)** physical mesh **b)** parametric mesh **c)** typical elements on single material without interface with C^1 continuity **d)** typical elements on material interface with C^0 continuity

In our optimization methodology, control points which define the geometry of the model, contain the nodal volume fractions of the reinforcement as optimization design variables. Note that this is an advantage due to the smoothness provided by the NURBS functions and the simplicity of dealing with only one approximation space for the geometry, reinforcement distribution and analysis. Though single knot insertion suffices to capture weak discontinuities

in the analysis of sandwich beam models using IGA, it does not properly represent the situation arising at the neighborhood of material interface in the reinforcement distribution surface. Assume that material interface is being C^0 continuous. Thus, according to Fig.2(d) there is a single row of control points (denoted by {27, 28, 29}) located at the interface in physical space. No control point can contain more than one value of nodal volume fraction of reinforcement as design variable in one optimization iteration. For element no. 3 corresponding control points are {21, 22, 23, 24, 25, 26, 27, 28, 29} and their counterpart design variables are {φ_{21}, φ_{22}, φ_{23}, φ_{24}, φ_{25}, φ_{26}, φ_{27}, φ_{28}, φ_{29}}. Analogously for element no. 4, {27, 28, 29, 30, 31, 32, 33, 34, 35} and {φ_{27}, φ_{28}, φ_{29}, φ_{30}, φ_{31}, φ_{32}, φ_{33}, φ_{34}, φ_{35}} are the vector of corresponding control points and the vector of design variables, respectively. Here {φ_{27}, φ_{28}, φ_{29}} are common design variables between element no. 3 and element no. 4. Since element no. 3 is located in face sheet and it is supposed that the face sheet material composition is fixed and does not change during the optimization, we set all design variables related to the face sheets to unity. So, {φ_{27}, φ_{28}, φ_{29}} as a part of the face sheet should be a unit vector. However, they also belong to element no. 4 in the core of the beam with different nodal values. To overcome this discrepancy, we impose C^{-1} continuity at the interface via the insertion of one additional knot (in total 3 knots at the parametric interface). In this case a new row of control points will coincide with the existing ones. Half of them contain the face sheet characteristics and the other half contains the core characteristics. Continuity in the displacement field along the interface is enforced by the penalty method. Fig.3 schematically illustrates the implemented technique. Red dots represent interfacial control points which are duplicated and coincident at the interfaces. Green ones show typical interior control points.
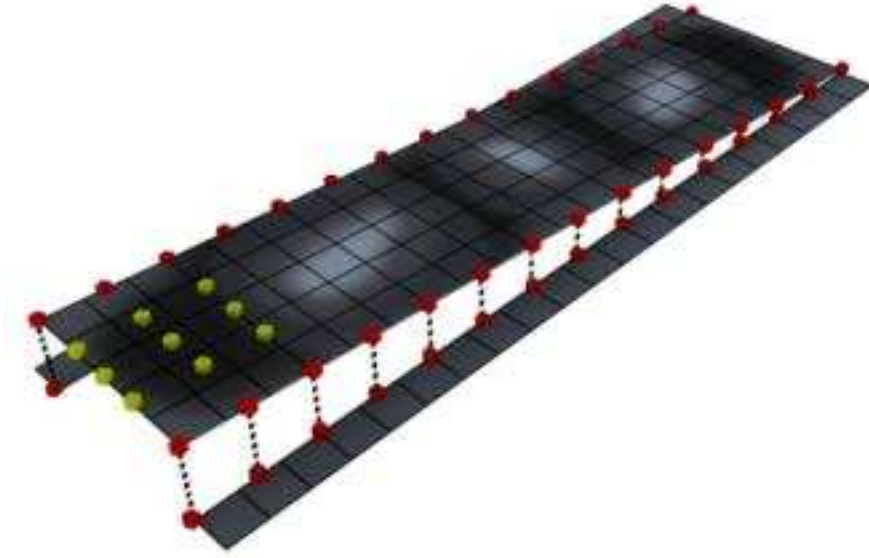
Fig.3 Exploded view of the sandwich beam modeled as multi-patches and glued with penalty method results in C^{-1} continuity. Interfacial control points are denoted by red dots and are coincident at interfaces. Green dots are typical interior control points.

5. Overview of optimization methodology

As mentioned before, NURBS basis functions are used in this work not only for the analysis but also to model the reinforcement distribution. In our methodology the nodal reinforcement volume fraction ($\varphi_{i,j}$) on control points are defined as design variables and the reinforcement distribution (η_p) is approximated as NURBS surface. Every point in the parametric space is mapped to the physical space having two attributes, geometrical coordinates and reinforcement volume fraction value. Due to the intrinsic characteristics of NURBS (higher order continuity and compact support, see [13]), even coarse meshes yield smooth enough surfaces to clearly represent the optimization results without needing any further image processing techniques [7].

The distribution function $\eta_p(x, y)$, which indicates the amount of reinforcement at every design point (x, y), is used for obtaining the homogenized stiffness. It is defined by:

$$\eta_p(x,y) = \sum_{i=1}^{n} \sum_{j=1}^{m} R_{i,j}^{p,q}(\xi,\eta)\ \varphi_{i,j} \qquad (11)$$

where $R_{i,j}^{p,q}$ are the NURBS basis functions. Once the reinforcement volume fraction at each point is available, the equivalent mechanical characteristics of the domain are obtained through the rule of mixtures:

$$C_{eq}(x,y) = (1 - \eta_p) \cdot C_m + \eta_p C_c \tag{12}$$

where C_{eq}, C_m and C_c are the homogenised, the matrix and the reinforcement elastic tensors, respectively. Subsequently, C_{eq} will be denoted by C. Since the core experiences mostly shear stresses, without loss of generality, the average value of the shear stresses within the area of interest is considered as the objective function. Other stress components (i.e. bending and peeling) can be also taken into account in the same manner. For the plane stress assumption, the stress in a vector form ($\boldsymbol{\sigma} = \{\sigma_{xx}, \sigma_{yy}, \sigma_{xy}\}$) is given by:

$$\boldsymbol{\sigma} = \boldsymbol{Tu} = \boldsymbol{CQu} \tag{13}$$

and also

$$\sigma_{xy} = \boldsymbol{t}_{xy}\boldsymbol{u} = \boldsymbol{C}_{xy}\boldsymbol{Qu} \tag{14}$$

where $\boldsymbol{T}$ is the stress matrix of the element, $(.)_{xy}$ is the related row of $(.)$ corresponding to the xy direction and $\boldsymbol{Q}$ is the matrix containing the derivatives of the shape functions. Thus, the objective function ($J(\boldsymbol{u}(\boldsymbol{\varphi}), \boldsymbol{\varphi})$) can be written in the following form:

$$J(\boldsymbol{u}(\boldsymbol{\varphi}), \boldsymbol{\varphi}) = \frac{1}{|\Omega_1|} \int_{\Omega_1} \sigma_{xy} d\Omega_1 \tag{15}$$

where Ω_1 is the area of interest over which the objective function is supposed to be minimized. The optimization problem can be summarized as follows:

Minimize: $\qquad\qquad\qquad\qquad J(\boldsymbol{u}(\boldsymbol{\varphi}), \boldsymbol{\varphi})$

Subjected to: $\qquad\qquad\qquad V_f = \int_\Omega \eta_p \, d\Omega \leq V_{f0} \tag{16}$

$$\boldsymbol{Ku} = \boldsymbol{f} \tag{17}$$

$$\varphi_{i,j} - 1 \leq 0 \tag{18}$$

$$-\varphi_{i,j} \leq 0 \tag{19}$$

V_f is the total reinforcement volume in each optimization iteration, V_{f0} is an arbitrary initial reinforcement volume which must be set at the beginning of the optimization process and Ω is the entire design domain; $\boldsymbol{K}$, $\boldsymbol{u}$ and $\boldsymbol{f}$ in Eq.(17) represent the global stiffness matrix of the system, the displacement and force vectors, respectively.

By introducing a proper Lagrangian objective function, l, and by using the Lagrangian multipliers method we have:

$$l = J - \left(V_f - V_{f0}\right) - \sum_{i,j=1}^{ncp} \psi_1\left(\varphi_{i,j} - 1\right) - \sum_{i,j=1}^{ncp} \psi_2\left(-\varphi_{i,j}\right) \tag{20}$$

where ψ_1, ψ_2 are upper and lower bounds values of the Lagrange multipliers, respectively. ncp is the number of control points. By setting the first derivative of Eq.(20) to zero we will obtain:

$$\frac{dl}{d\boldsymbol{\varphi}} = \frac{dJ}{d\boldsymbol{\varphi}} - \frac{dV_f}{d\boldsymbol{\varphi}} - \psi_1 + \psi_2 = 0 \tag{21}$$

$\boldsymbol{\varphi}$ denotes the vector containing all $\varphi_{i,j}$. In this work we implement optimality criteria (OC) based optimization (Zhou & Rozvany, 1991, [19]) to numerically solve Eq.(21). The design variables are updated by a sensitivity analysis as presented next.

5.1 Adjoint sensitivity analysis

In gradient-based methods, to solve Eq.(21), one should differentiate the objective and constraint functions with respect to the design variables. The procedure to obtain these derivatives is called sensitivity analysis. Generally, there are two main groups of methods for sensitivity analysis: numerical methods (e.g. finite difference) which are approximate; and analytical methods (including direct and adjoint methods) which are exact. According to [20] the most efficient method for calculating derivatives involved in Eq.(21) is the adjoint method since there is a large number of design variables but few functions (here two, including objective function and design constraint). Recalling Eq.(21), we use the chain-rule to calculate the sensitivity of $J(\boldsymbol{u}(\boldsymbol{\varphi}), \boldsymbol{\varphi})$ with respect to $\boldsymbol{\varphi}$ using partial derivatives ($\frac{\partial(.)}{\partial(.)}$):

$$\frac{dJ}{d\boldsymbol{\varphi}} = \frac{\partial J}{\partial \boldsymbol{u}} \frac{\partial \boldsymbol{u}}{\partial \boldsymbol{\varphi}} + \frac{\partial J}{\partial \boldsymbol{\varphi}} \tag{22}$$

From force equilibrium we have:

$$\left(\frac{\partial \boldsymbol{f}}{\partial \boldsymbol{u}}\right)^T \frac{\partial \boldsymbol{u}}{\partial \boldsymbol{\varphi}} + \frac{\partial \boldsymbol{f}}{\partial \boldsymbol{\varphi}} = 0 \tag{23}$$

$$\frac{\partial \boldsymbol{u}}{\partial \boldsymbol{\varphi}} = -\left(\frac{\partial \boldsymbol{f}}{\partial \boldsymbol{u}}\right)^{-T} \frac{\partial \boldsymbol{f}}{\partial \boldsymbol{\varphi}} \tag{24}$$

where $(.)^T$ denotes transpose of $(.)$. Substitution of Eq.(24) in Eq.(22) yields to:

12

$$\frac{dJ}{d\boldsymbol{\varphi}} = -\frac{\partial J}{\partial \boldsymbol{u}} \left[\left(\frac{\partial \boldsymbol{f}}{\partial \boldsymbol{u}}\right)^{-T} \frac{\partial \boldsymbol{f}}{\partial \boldsymbol{\varphi}} \right] + \frac{\partial J}{\partial \boldsymbol{\varphi}} \tag{25}$$

By assuming

$$\boldsymbol{\lambda} = -\frac{\partial J}{\partial \boldsymbol{u}} \left(\frac{\partial \boldsymbol{f}}{\partial \boldsymbol{u}}\right)^{-T} \tag{26}$$

and knowing that $\frac{\partial \boldsymbol{f}}{\partial \boldsymbol{u}} = \boldsymbol{K}$, we can write:

$$\boldsymbol{K}\boldsymbol{\lambda} = -\frac{\partial J}{\partial \boldsymbol{u}} \tag{27}$$

Eventually Eq.(22) can be written in the form:

$$\frac{dJ}{d\boldsymbol{\varphi}} = (\boldsymbol{\lambda})^T \frac{\partial \boldsymbol{f}}{\partial \boldsymbol{\varphi}} + \frac{\partial J}{\partial \boldsymbol{\varphi}} \tag{28}$$

The second terms of Eq.(28) are obtained as follows:

$$\frac{\partial J}{\partial \boldsymbol{\varphi}} = \frac{1}{|\Omega_1|} \int_{\Omega_1} \frac{\partial \boldsymbol{C}_{xy}}{\partial \boldsymbol{\varphi}} \boldsymbol{Q} \, \boldsymbol{u} \, d\Omega_1 \tag{29}$$

with

$$\frac{\partial \boldsymbol{C}_{xy}}{\partial \boldsymbol{\varphi}} = -\frac{\partial \eta_p}{\partial \boldsymbol{\varphi}} \cdot \boldsymbol{C}_{m_{xy}} + \frac{\partial \eta_p}{\partial \boldsymbol{\varphi}} \cdot \boldsymbol{C}_{c_{xy}} \tag{30}$$

$\boldsymbol{C}_{m_{xy}}$ and $\boldsymbol{C}_{c_{xy}}$ in right hand side of Eq.(30) are related rows of $\boldsymbol{C}_m$ and $\boldsymbol{C}_c$ corresponding to the

shear (xy) component. Considering Eq.(11), one can write:

$$\frac{\partial \eta_p}{\partial \varphi_{i,j}} = R_{i,j}^{p,q}(\xi, \eta) \tag{31}$$

To complete Eq.(28), $\frac{\partial J}{\partial \boldsymbol{u}}$ and $\frac{\partial \boldsymbol{f}}{\partial \boldsymbol{\varphi}}$ are needed:

$$\frac{\partial J}{\partial \boldsymbol{u}} = \frac{1}{|\Omega_1|} \int_{\Omega_1} \boldsymbol{C}_{xy} \boldsymbol{Q} \, d\Omega_1 \tag{32}$$

and

$$\frac{\partial \boldsymbol{f}}{\partial \boldsymbol{\varphi}} = \int_{\Omega} \frac{\partial \boldsymbol{K}}{\partial \boldsymbol{\varphi}} \boldsymbol{u} \, d\Omega \tag{33}$$

where

$$\frac{\partial \boldsymbol{K}}{\partial \boldsymbol{\varphi}} = \int_{\Omega} \boldsymbol{Q}^T \frac{\partial \boldsymbol{C}_{eq}}{\partial \boldsymbol{\varphi}} \boldsymbol{Q} \, d\Omega \tag{34}$$

Finally, the second term of Eq.(21) can be written as:

$$\frac{dV_f}{d\boldsymbol{\varphi}} = \frac{\partial V_f}{\partial \boldsymbol{\varphi}} = \int_{\Omega} \frac{\partial \eta_p}{\partial \boldsymbol{\varphi}} \, d\Omega \tag{35}$$

where $\frac{\partial \eta_p}{\partial \boldsymbol{\varphi}}$ can be obtained from Eq.(31).

6. Case studies

In this section, the NURBS-based finite element model is verified by performing both static and dynamic benchmark problems. Afterwards the performance of the optimization algorithm is studied.

6.1 Verification of the IGA model

6.1.1 Static analysis of a sandwich beam with a homogeneous elastic core

To demonstrate the accuracy and convergence of the IGA model, in particular with respect to the imposed discontinuity at the interface, we first analyze a sandwich beam as sketched in Fig.4 under $100 \, N/m$ uniform distributed load at the top of the beam. The beam is $4.8m$ long and $1.2m$ wide and clamped at the left edge. The design parameters are listed in Table-1. The model is discretized by a 21×12 quadratic NURBS mesh.
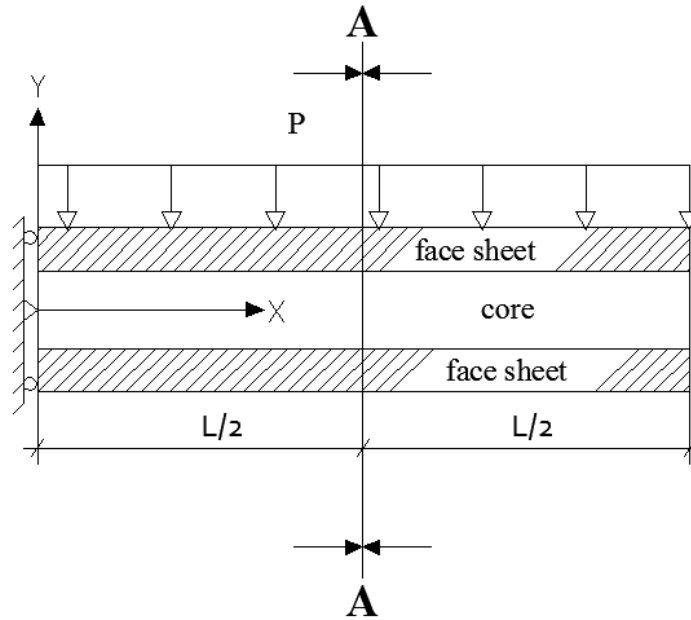

Fig.4 Model of the cantilever sandwich beam

Table-1 Design data of the sandwich beam with a homogeneous elastic core

Property	Elastic Core	Face Sheets
Young's Modulus E(GPa)	0.167	1.67
Poisson's ratio (ν)	0.3	0.3
Thickness (CM)	0.8	0.2

Fig.5 and Fig.6 show the solution for the displacements and the stresses at the middle section $x = L/2$ (cut **A-A** in Fig.4). As can be observed from the graphs, displacements are continuous as required by the compatibility condition. The jump in σ_{xx} is properly reproduced at the interfaces as well as the slope discontinuity in shear stresses, σ_{xy} . The results agree well with the benchmark problem in [21].

a)   b)
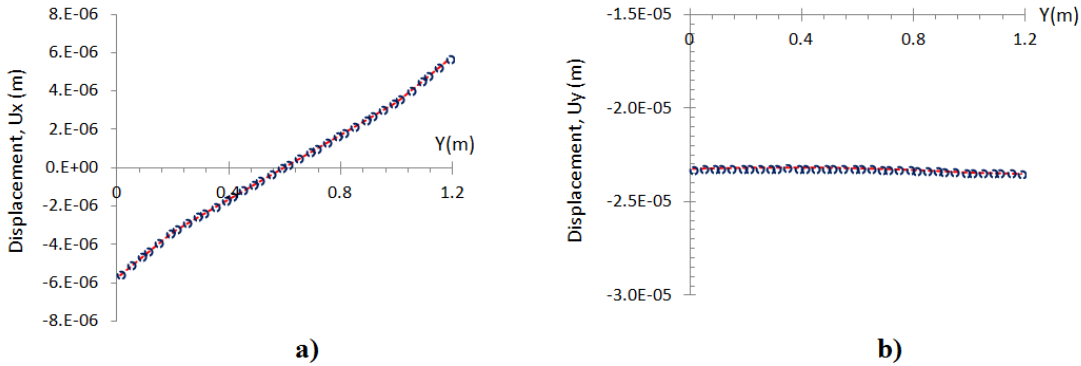
Fig.5 Displacements in the x (**a**) and y direction (**b**) of a sandwich cantilever beam along cut *A-A* ($x = \frac{L}{2}$) shown in Fig.4


a)   b)
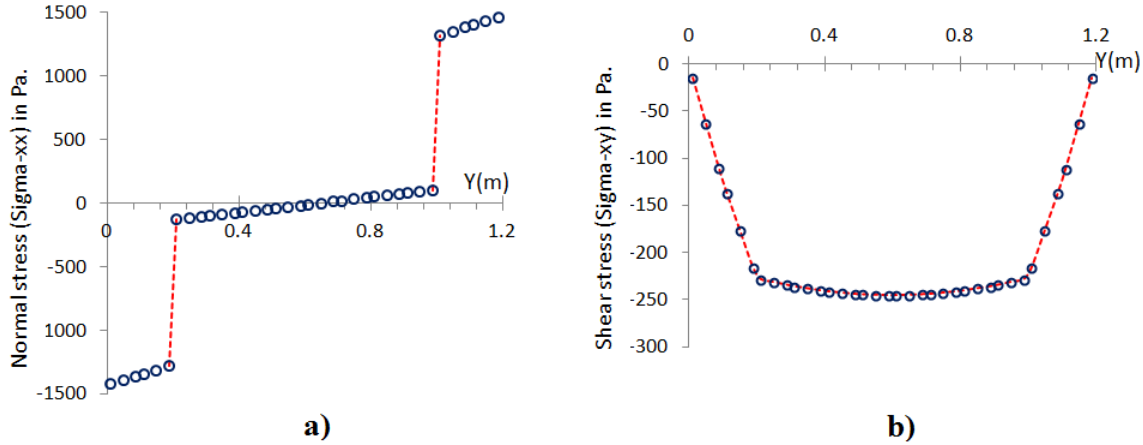
Fig.6 Normal stress (**a**) and shear stress (**b**) in a sandwich cantilever beam along cut *A-A* ($x = \frac{L}{2}$) shown in Fig.4

15

Replacing the distributed load a parabolic traction at right edge of the beam, the displacement and energy norms are evaluated by

$$e_{energy} = \left[\frac{1}{2} \int_{\Omega} (\boldsymbol{\epsilon}_{num} - \boldsymbol{\epsilon}_{exact}).\boldsymbol{D}.(\boldsymbol{\epsilon}_{num} - \boldsymbol{\epsilon}_{exact})d\Omega \right]^{\frac{1}{2}} \tag{36}$$

$$e_{displacement} = \left\{ \frac{\int_{\Omega} [(\boldsymbol{u}_{num} - \boldsymbol{u}_{exact}).(\boldsymbol{u}_{num} - \boldsymbol{u}_{exact})]d\Omega}{\int_{\Omega} [\boldsymbol{u}_{exact} \cdot \boldsymbol{u}_{exact}]d\Omega} \right\}^{\frac{1}{2}} \tag{37}$$

where $\boldsymbol{\epsilon}$ and $\boldsymbol{u}$ are the strain and displacement vectors while the subscripts $_{num}$ and $_{exact}$ denote "numerical" and "exact", respectively. The exact displacements as derived in [22] are imposed on the entire boundary of the beam using the least squares method (see [23]). The convergence results are shown in Fig.7. The mesh parameter h is defined as the ratio between the beam height and the number of elements in the vertical direction. Using quadratic mesh, the optimal convergence rates (three for displacement norm and two for energy norm) are obtained.
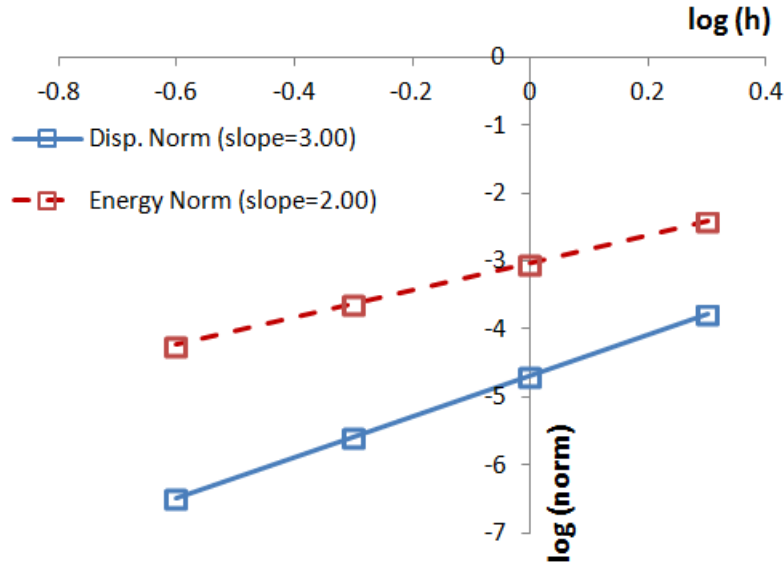
Fig.7 Energy and displacement norms for the sandwich cantilever beam under parabolic loading at the right edge

6.1.2 Free vibration of a sandwich beam with a FG core

This example includes a sandwich beam with the FG core made of Aluminum and Zirconia (Al/Zro2). The length of the beam is $L = 200$ mm, its height is $D = 20$ mm and the core thickness is $t_c = 14$ mm. Other relevant data is listed in Table-2. Geometry, loading and support conditions are as in Fig.4.

Table-2 Material properties of the sandwich beam with the FG core

Property	Aluminum	Zirconia	Face sheets
Young's Modulus E(GPa)	70	151	210
Poisson's ratio (v)	0.3	0.3	0.3
Mass density ($\frac{kg}{m^3}$)	2700	5700	7860

Table-3 shows the first six natural frequencies of the sandwich beam with the FG core. Results obtained by other methods [9] are also presented. Using IGA with coarse meshes yields to accuracy around 0.1% comparing with reference results (fine mesh FEM using ANSYS) as presented in Table-3.

Table-3 The first six natural frequencies for a sandwich beam with FG core

Mode	Mori-Tanaka					ROM Tech.				
	t-RPIM	IGA	t-RPIM	IGA	FEM (ANSYS)	t-RPIM	IGA	t-RPIM	IGA	FEM (ANSYS)
	21 x 11		101 x 11		-	21 x 11		101 x 11		-
1	461.7	458.01	459.2	457.8	458.2	461.5	459.28	459.4	459.02	459.5
2	2729.4	2695.65	2709.2	2694.1	2697.1	2727.8	2707.1	2708.7	2705.5	2708.6
3	6443.7	6368.67	6432.9	6367.4	6374.1	6443.0	6436.0	6440.7	6434.7	6440.8
4	7105.9	6944.8	6954.7	6940.0	6950.2	7065.4	6985.8	6995.8	6981.1	6991.3
5	12651.9	12341.3	12462.2	12330	12353	12634.2	12434.5	12446.4	12423	12446.0
6	18999.3	18465.8	18594.6	18441	18483	18990.8	18630.4	18659.5	18606	18647.0

Though, the aim of this paper is not to demonstrate the advantages of IGA in sandwich beam modeling, Fig.8 shows smooth convergence of the NURBS results. This coarse model accuracy is beneficial for iterative design procedure and optimization especially when FE model is computationally expensive.
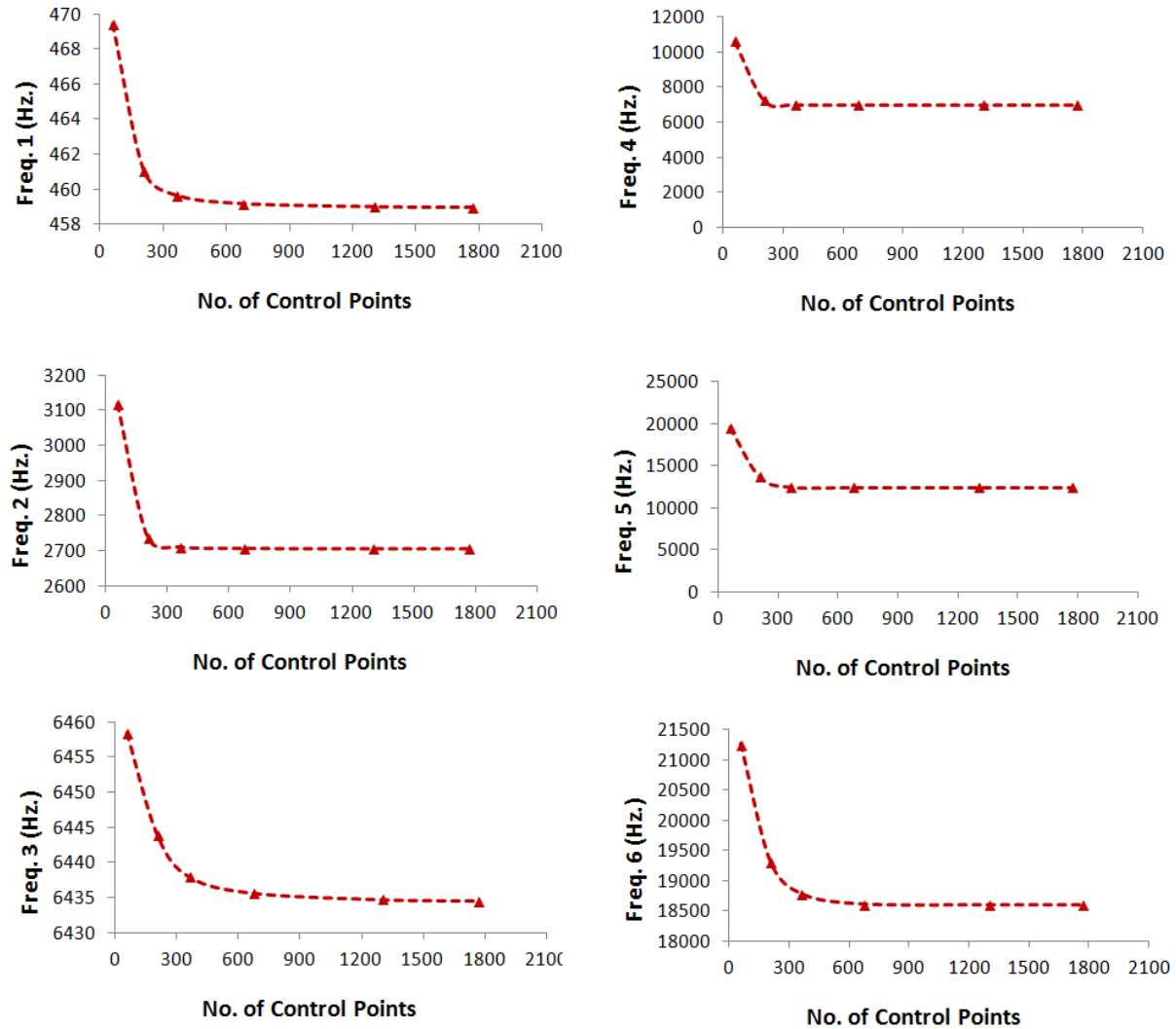
Fig.8 The first six natural frequencies of the sandwich beam with FG core versus number of control points of the model

6.2 Optimization case studies

After the verification of the IGA model, we proceed to the optimization of the reinforcement distribution. Let us consider again the cantilever sandwich beam with uniformly distributed load as shown in Fig.4. All design parameters are summarized in Table-4.

Fig.9 illustrates the chosen sub-domains which are considered for the definition of the objective function. Areas are considered at mid span, mid height and in the vicinity of the interfaces. As mentioned before, since core shearing and debonding failure states are mostly due

to shear stresses, we concentrate on the minimization of the shear stresses. However, other components of the stresses can be also taken into account.

Table-4 Problem definition, cantilever sandwich beam with uniformly distributed top load

L_x	L_y	E_m	E_c	E_f	ν	P	t_f	t_c	V_c	V_{cmax}
1.25	0.25	3.5	72.4	210	0.3	10	0.025	0.2	10%	60%

L_x, L_y, t_f, t_c: $Beam\ length, thickness, face\ thk.\ and\ core\ thk. (m),\ V_c : total\ reinforc. vol.,$

$E_m,\ E_c,\ E_f$: $Young's\ modulus\ of\ matrix, reinforcement\ and\ face\ sheet\ (GPa)$

P: $Applied\ load\ \left(\dfrac{KN}{m}\right),\ \ \nu$: $Poisson\ ratio,\ V_{cmax}\ : the\ maximum\ nodal\ reinforcement$
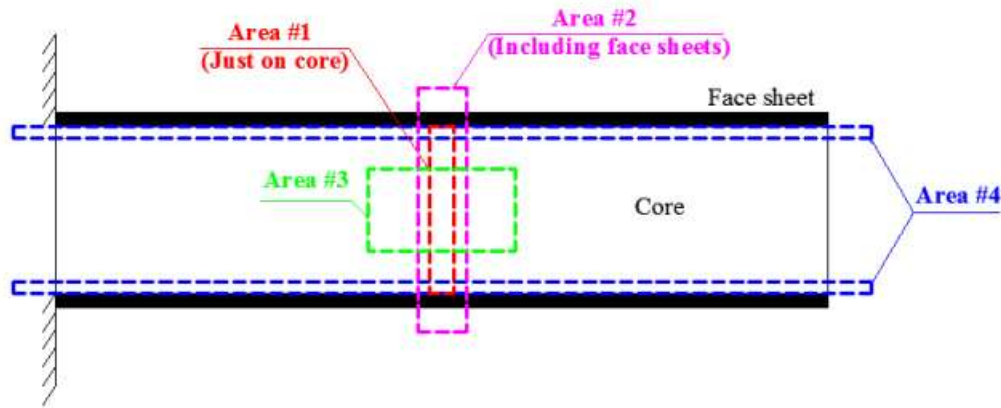

Fig.9 Definition of area of interest

Fig.10(a) depicts the optimal layout of the reinforcement distribution in the core minimizing the shear stresses inside the area of interest #1. Fig.10(b) shows the evolution of the objective function during the iterative process. The shear stress inside the nominated sub-domain, converges smoothly towards a minimum value.
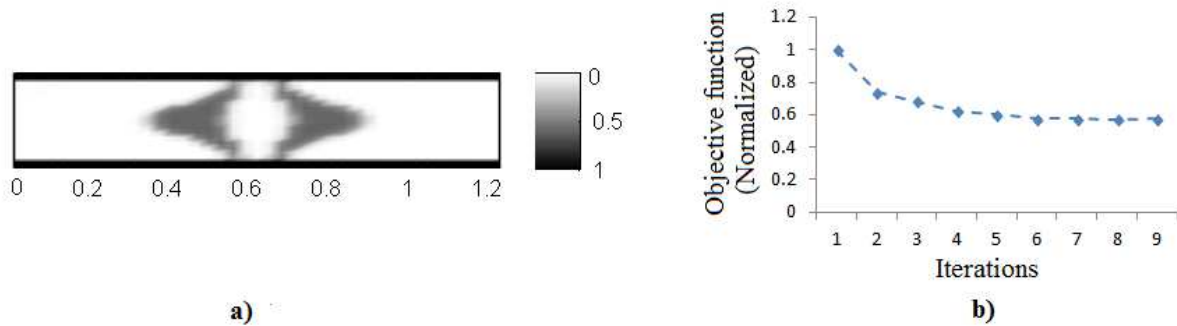
Fig.10 Optimal distribution of reinforcing ingredients considering area of interest #1 **(a)**, objective function versus iterations **(b)**

Fig.11 compares the shear stress across the thickness of the beam at mid of area #1 considering homogeneous and optimal distributions of reinforcements. The graph clearly shows that the shear stress profile improves inside the area of interest (around 50% reduction); however, for the face sheets which are outside area of interest #1(dash lines), the shear stress increases.
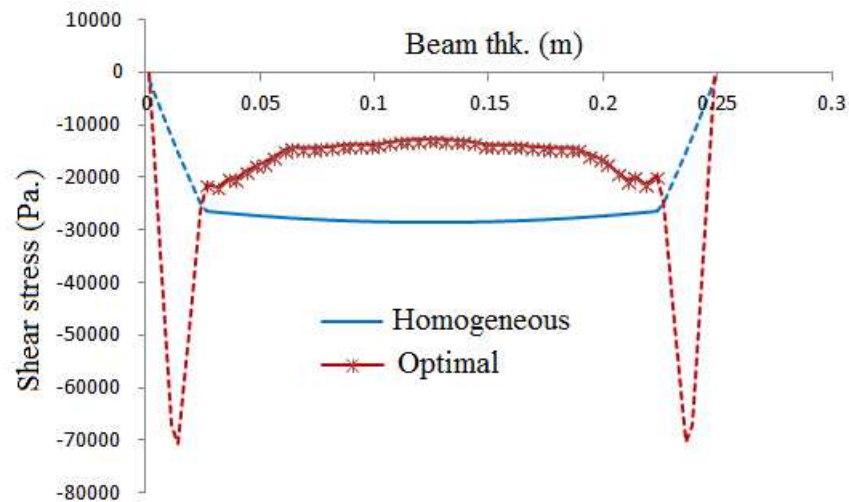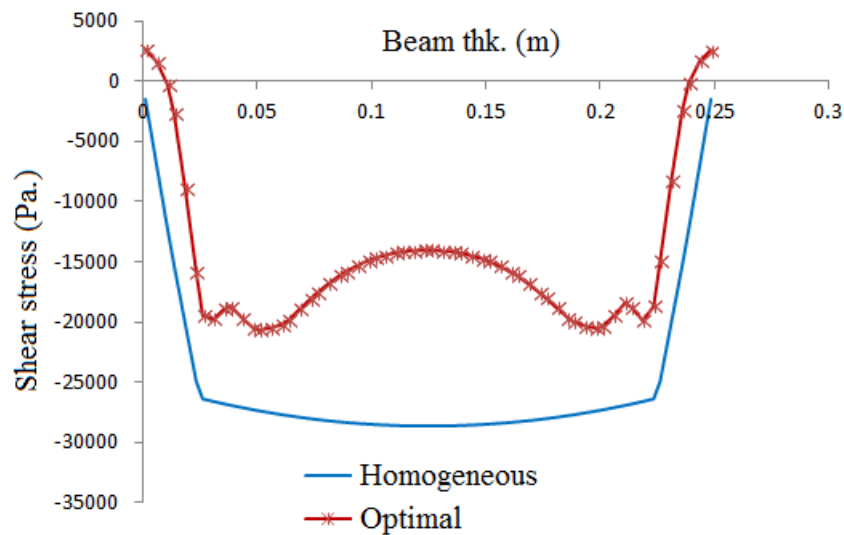

Fig.11 Shear stress profile for area #1 considering homogeneous and optimal distribution of reinforcements, dash lines stand for face sheets which are outside of area #1

To demonstrate the correctness of the model, we extend area of interest #1 to include face sheets. The extended area is called area of interest #2 (see Fig.9). The optimal distribution of the reinforcement and the history of objective function are plotted in Fig.12(a) and 12(b),

respectively. Fig.13 compares the shear stress profiles before and after optimization. As expected, the shear stresses improve within area #2.
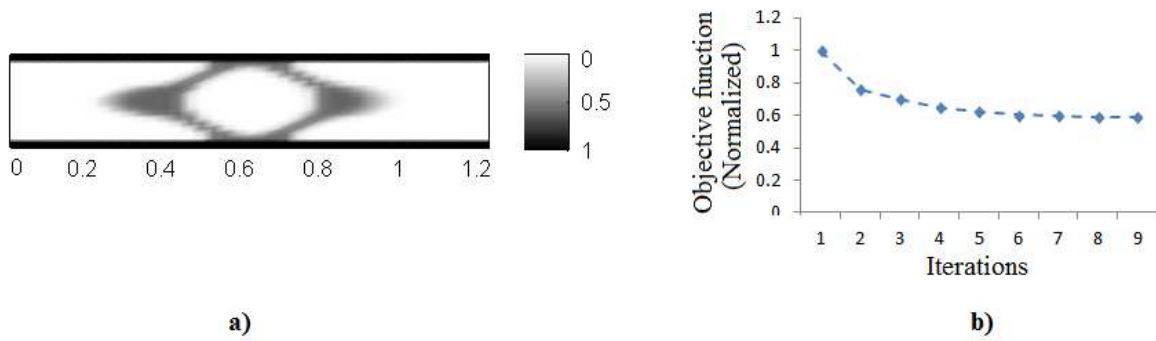

a)

b)
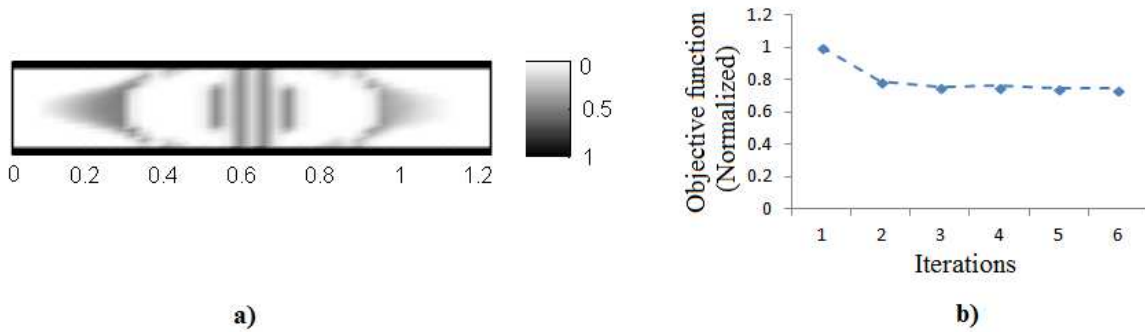
Fig.12 Optimal distribution of reinforcing ingredients considering area of interest #2 **(a)**, objective function versus iterations **(b)**
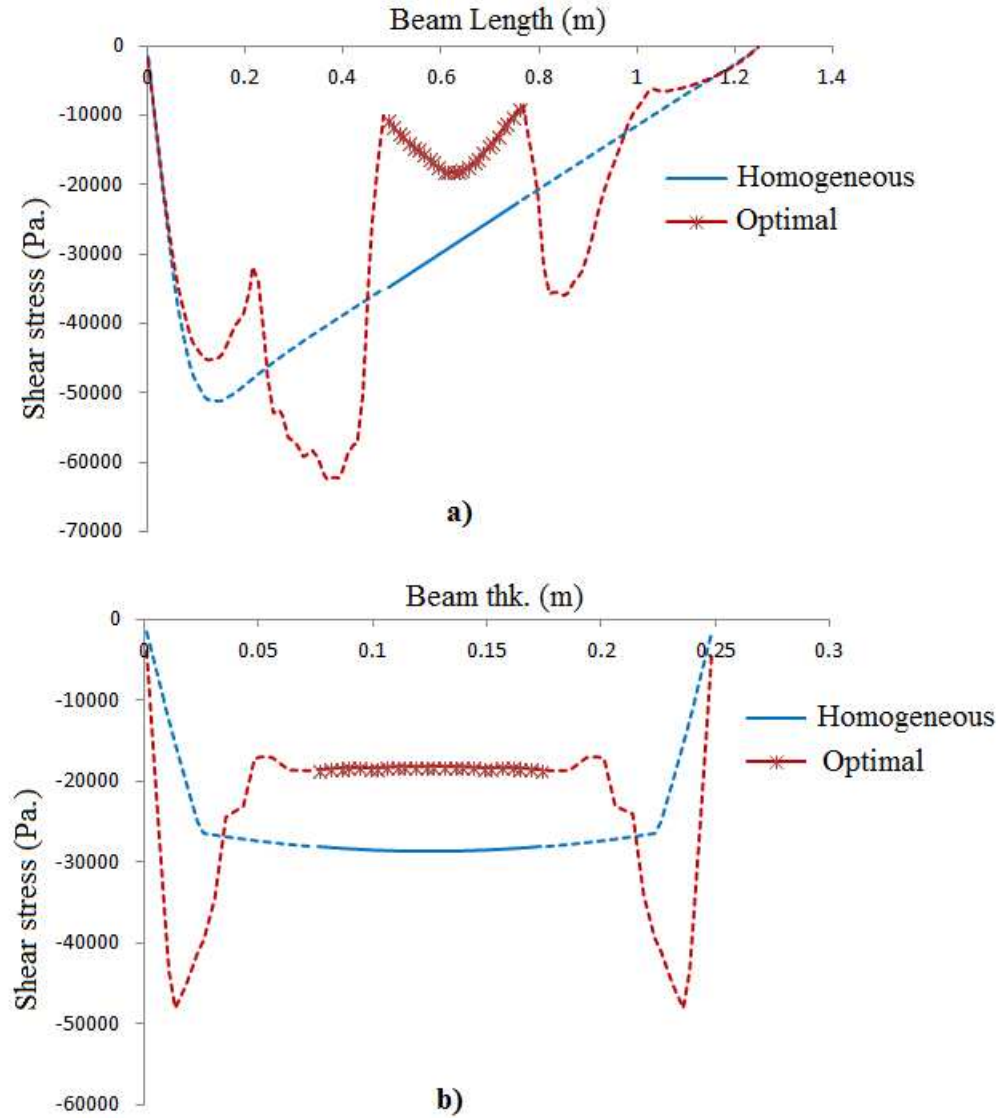

Fig.13 Shear stress profile for area #2 considering homogeneous and optimal distribution of reinforcements

In the next case, area of interest #3 is defined on the core of the beam and includes central elements of the core as illustrated in Fig.9. The same types of results are presented in Fig.14(a) and 14(b).
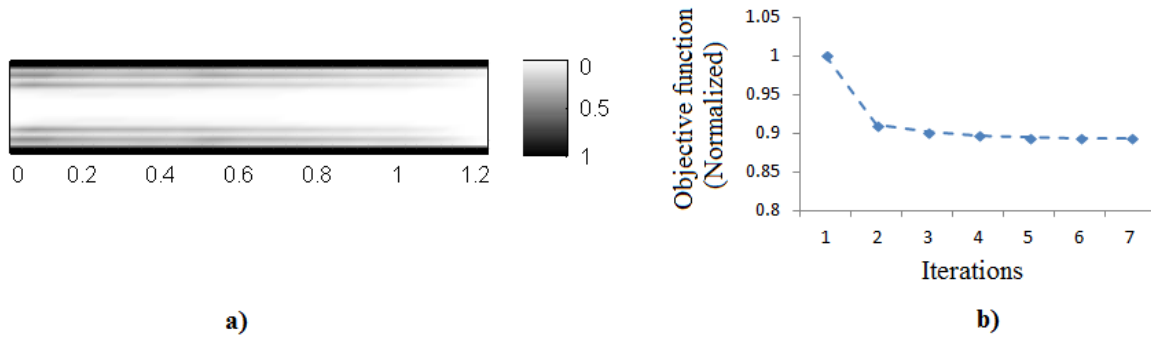
Fig.14 Optimal distribution of reinforcing ingredients considered area of interest #3 **(a)**, objective function versus iterations **(b)**

Fig.15 shows the shear stress profile before and after optimization along a section at mid width (Fig.15(a)) and mid span (Fig.15(b)). In both figures, dash lines refer to zones which are outside the interested area #3. Again, the graphs clearly illustrate that the shear stresses considerably decrease in the area of interest.

Fig.15 Shear stress profile for area #3 along a section at mid width **(a)** and mid length **(b)** of the beam considering homogeneous and optimal distribution of reinforcements. In both figures, dash lines refer to zones which are outside the interested area #3.

As a final case, we consider area of interest #4 which includes interfacial elements in core of the beam (see Fig.9). The optimal distribution of reinforcing ingredients and the history of the objective function are illustrated in Fig.16(a) and 16(b), respectively.

Fig.16 Optimal distribution of reinforcing ingredients considering area of interest #4 **(a)**, objective function versus iterations **(b)**

Fig.17 compares the shear stress at the interfacial elements of the core along the length of the beam. Fig.17(a) is for the bottom interface and Fig.17(b) is for the top interface. In both graphs dashed lines show the shear stress for pure polymer (without any reinforcements). Adding 10% uniformly distributed reinforcing ingredients to the polymer matrix negligibly improves the shear stresses along the interfaces, while the same amount of reinforcements with optimal distribution, considerably reduces the interfacial shear stresses. This improvement has descending trend from the fixed left end (with the maximum shear load) to the free right end (with zero shear load).

The results in Fig.17 are based on averaging shear stress inside each element. The similar results are presented in Fig.18 by plotting nodal values of shear stress along longitudinal sections cutting through the area of interest #4. Fig.18(a) and 18(b) correspond to the top and the bottom interfaces, respectively. These graphs prove that the beam with uniform FRP doesn't show considerable improvement in interfacial shear stress in comparison with pure polymer; while dominant improvement needs to optimal distribution of reinforcements.

24
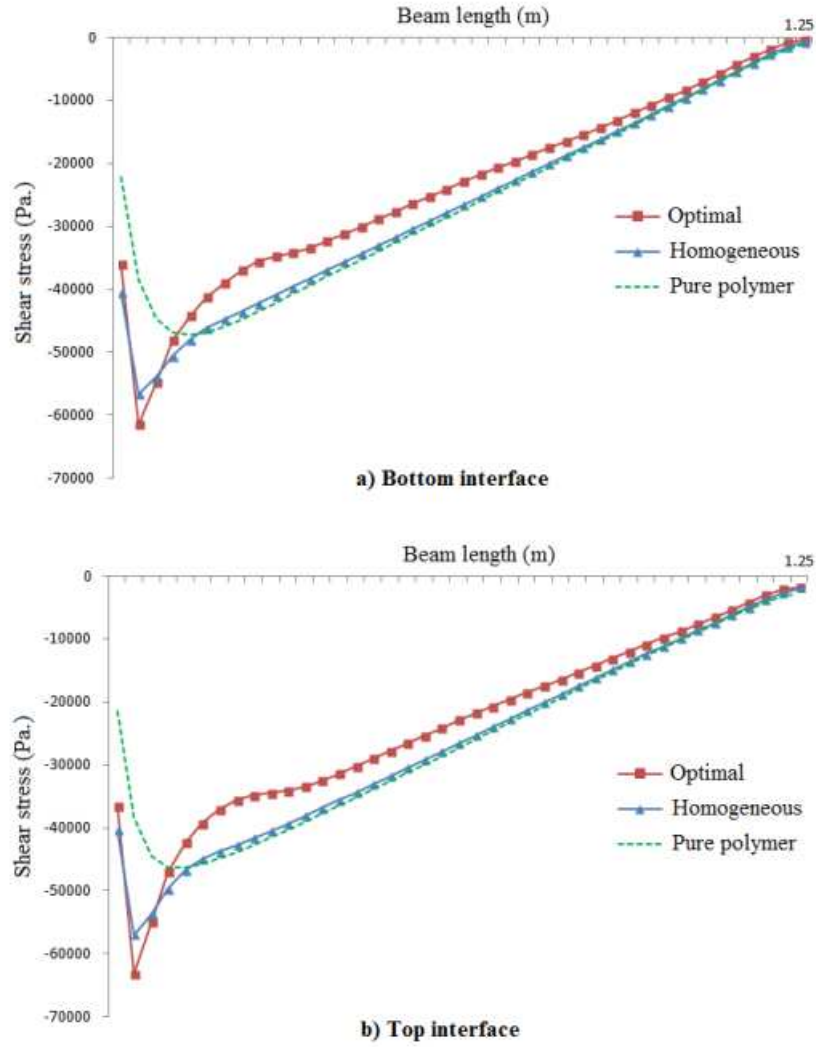
Fig.17 Average of shear stress in each interfacial element along the beam length considering area of interest #4 for pure polymer, homogeneous FRP and FRP with optimal distribution of reinforcements for **(a)** bottom interface and **(b)** top interface
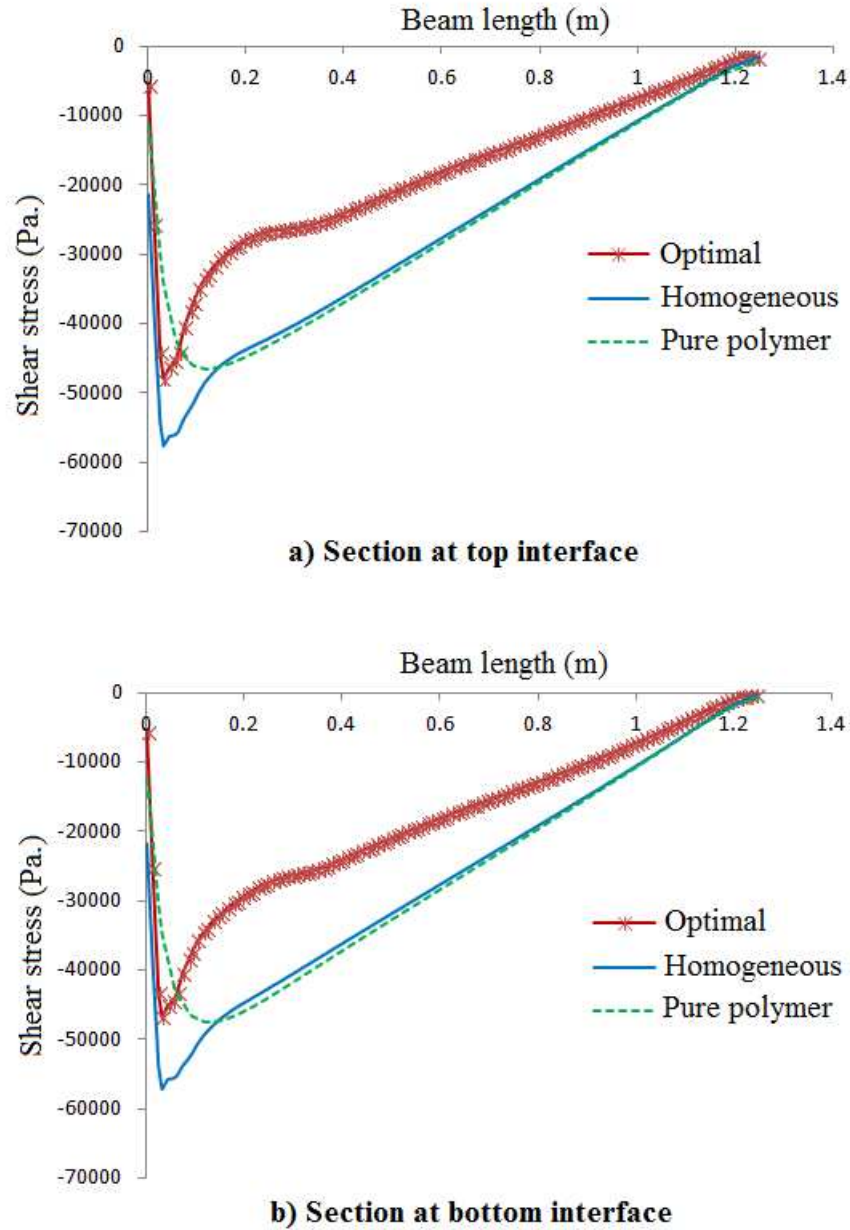
Fig.18 Nodal values of shear stress along a longitudinal sections at top interface **(a)** and bottom interface **(b)** in area of interest #4 comparing characteristics obtained by pure polymer, homogeneous FRP and FRP with optimal distribution of reinforcements

7. Concluding remarks

Excessive shear stress in sandwich beams can yield to core shearing and core/face debonding. This research work presents a computational algorithm for decreasing interfacial shear stress in

sandwich beams with polymeric core. The output of the algorithm is the optimal distribution of reinforcing ingredients inside the polymer matrix. The algorithm can be also used for optimizing other stress components (i.e. peeling and bending stresses) in any arbitrary zone of the design domain. Our methodology takes advantages of NURBS basis functions for both analysis (IGA) and reinforcement distribution optimization (NURBS surface). Using IGA for model analysis, yields to high rate and smooth convergence to exact results. C^{-1} continuity is imposed at the interface to "truly" isolate the reinforcement distribution in the core from the face sheets using multi-patch and penalty techniques. The adjoint sensitivity technique provides flexibility in defining the area of interest over which the objective function is minimized and also for efficient updating of the design variables through optimization iterations. Comparing the results of the case study illustrates that adding reinforcements homogeneously into polymers will slightly improve the interfacial shear stress but that considerable improvements are observed when the distribution of the reinforcement in the core is optimized.

Acknowledgments:

References:

1. Manalo AC, Aravinthan T, Karunasena W. Flexural behavior of laminated fiber composite sandwich beams. Proceedings of the second official international conference of international institute for FRP in construction for Asia-Pacific region, Seoul, 9-11 December 2009. P. 407-412.
2. Hu H, Belouettar S, Ferry MP, Daya EM. Review and assessment of various theories for modeling sandwich composites. Composite Structures 2008; 84:282-292.
3. Triantafillou TC, Gibson LJ. Debonding in foam-core sandwich panels. Materials and structures 1989; 22:64-69.
4. Jha DK, Kant T, Singh RK. A critical review of recent research on functionally graded plates. Composite Structures 2013; 96:833-849.
5. Krour B, Bernard F, Tounsi A. Fibers orientation optimization for concrete beam strengthened with a CFRP bonded plate: A coupled analytical–numerical investigation. Engineering structures 2013; 56:218-227.
6. Lousdad A, Megueni A, Bouchikhi AS. Geometric edge shape based optimization for interfacial shear stress reduction in fiber reinforced polymer plate retrofitted concrete beams. Computational material science 2010; 47:911-918.

7. Ghasemi H, Brighenti R, Zhuang X, Muthu J, Rabczuk T. Optimization of fiber distribution in fiber reinforced composite by using NURBS functions. Computational material science 2014; 83:463-473.

8. Mori T, Tanaka K. Average stress in matrix and average elastic energy of materials with mis-fitting inclusions. Acta Metal. 1973; 21:571-583.

9. Bui TQ, Kosravifard A, Zhang CH, Hematiyan MR, Golub MV. Dynamic analysis of sandwich beam with functionally graded core using a truly meshfree radial point interpolation method. Engineering structures 2013; 47:90-104.

10. Hughes TJR, Cottrell JA, Bazilevs Y. Isogeometric Analysis: CAD, finite elements, NURBS, exact geometry and mesh refinement. Comput. Methods Appl. Mech. Eng. 2005; 194:4135-4195.

11. Lian H, Simpson RN, Bordas SPA. Shape optimization for three dimensional linear elasticity using an isogeometric boundary element method with T-splines. Proceedings of the International Conference on Computational Mechanics, Durham, 2013.

12. Lian H, Simpson RN, Bordas SPA. Sensitivity analysis and shape optimization with the isogeometric boundary element method. Proceedings of the 20th UK Conference of the Association for Computational Mechanics, Manchester, 2012.

13. Cottrell JA, Hughes TJR, Bazilevs Y. Isogeometric Analysis towards integration of CAD and FEA. Wiley, UK, 2009

14. Duddu R, Bordas SPA, Chopp D, Moran B. A combined extended finite element and level set method for biofilm growth. Int. J. Numer. Meth. Engng. 2008; 74(5):848-870.

15. Zhao X, Bordas SPA, Qu J. A hybrid smoothed extended finite element/level set method for modeling equilibrium shapes of nano-inhomogeneities. Comput Mech. 2013; 52:1417-1428.

16. Ghorashi SS, Valizadeh N, Mohammadi S. Extended isogeometric analysis for simulation of stationary and propagating cracks. Int. J. Numer. Meth. Engng. 2012; 89:1069-1101.

17. Jia Y, Anitescu C, Ghorashi SS, Rabczuk T. Extended isogeometric analysis for material interface problems. IMA Journal of Applied Mathematics 2014; Xx:xx-xxx. DOI:10.1093/imamat/hxu004.

18. Nguyen VP, Kerfriden P, Bordas SPA. Two- and three-dimensional isogeometric cohesive elements for composite delamination analysis. Composites Part B: Engineering 2014; 60:193-212.

19. Zhou M., Rozvany GIN. The COC algorithm part II: topological, geometry and generalized shape optimization. Comput. Methods Appl. Mech. Eng. 1991; 89:197-224.

20. Bendsoe MP, Sigmund O. Topology optimization:Theory, Methods, and Applications. Springer, Germany, 2003.

21. Zong Z, Lam KY, Zhang YY. The multidomain differential quadrature approach to plane elastic problems with material discontinuity. Mathematical and computer modeling 2005;41:539-553.

22. Liu GR, Wang Z, Zhang GY, Zong Z, Wang S. An Edge-Based Smoothed Point Interpolation Method for Material Discontinuity. Mechanics of Advanced Materials and Structures 2012; 19(1-3):3-17.

23. Nguyen VP, Rabczuk T, Bordas SPA. Isogeometric analysis: An overview and computer implementation aspects. Mathematics and Computers in Simulation; Submitted.